Journal of the Optical Society of America B
OPTICAL PHYSICS

Broadband XUV supercontinuum generation by time-dependent phase-matching

FENG WANG,[1] FANG LI,[1,2,3] AND ZHE WANG[2,4]

[1]School of Physics and Wuhan National Laboratory for Optoelectronics, Huazhong University of Science and Technology, Wuhan 430074, China
[2]Laboratory of Optical Information Technology, Wuhan Institute of Technology, Wuhan 430205, China
[3]e-mail: lifang_wit@hotmail.com
[4]e-mail: acdcvy1988@163.com

Received 9 May 2016; revised 24 June 2016; accepted 30 June 2016; posted 30 June 2016 (Doc. ID 264752); published 15 July 2016

We investigate the influence of the time-dependent on-axis phase matching on broadband extreme ultraviolet (XUV) supercontinuum generation with an intense laser field. By using the strong-field approximation model and solving Maxwell's equations we show that time-dependent on-axis phase matching can lead to broadening of the XUV supercontinuum. Moreover, we also demonstrate that the bandwidth of the XUV supercontinuum can be controlled by adjusting the beam waist of the laser field and the position of the gas medium.

OCIS codes: (190.7110) Ultrafast nonlinear optics; (190.4160) Multiharmonic generation; (190.2620) Harmonic generation and mixing.

http://dx.doi.org/10.1364/JOSAB.33.001688

1. INTRODUCTION

High-order harmonic generation (HHG) [1] is a widespread technique for the generation of attosecond pulses. The unprecedented resolution of attosecond pulses makes it possible to study the ultrafast electron dynamics in atoms [2–8], molecules [9–13], and solids [14] as well as for time-resolved metrology and spectroscopy [15–19]. Due to these potential applications, the generation of isolated attosecond pulses based on HHG has gained extensive attention.

The HHG process can be well understood in terms of the three-step model [20]: ionization, acceleration, and recombination. This process periodically occurs every half optical cycle of the laser field and produces two attosecond pulses in each optical cycle. Based on this classical picture many methods have been used to control the harmonic emission within a half optical cycle of the laser field for the isolated attosecond pulse generation such as, by using a sub-4 fs near-single-cycle driving pulse [21], a pulse as short as 80 attoseconds has been generated by synthesizing harmonics near the cutoff region. The polarization gating technique [22–26] has also been demonstrated to produce a broadband supercontinuum in the plateau region. Some other ways such as two-color field [27–32], multicolor field [33], ionization gating [34], and double optical gating [35] have also been reported for the generation of the isolated attosecond pulses.

A full knowledge of the HHG depends not only on the laser-atom interaction on the single-atom level, but also on the propagation and phase matching in the macroscopic medium. Previous studies of the HHG in macroscopic gases mainly focus on the different phase-matching properties of the short and long paths. Many works have been done to achieve the quantum path selection [36–39] and investigate the complex spatial structures in the harmonic spectra [40–43]. On the other hand, since the HHG is an ultrafast process, phase matching accompanying the HHG evolves quickly with time. The time dependence of the phase matching [44–49] plays a dramatic role in the HHG. Recently, by using a high gas pressure and low laser intensity, Chen *et al.* [50] demonstrated that the phase matching of HHG can be restricted to one half optical cycle, and then an isolated attosecond pulse can be produced within this temporal phase-matching window.

In this paper, we investigate the influence of the time-dependent on-axis phase matching on XUV supercontinuum generation in a high-intensity and low-pressure regime. Based on the numerical simulation of Maxwell's equations we show that the time-dependent on-axis phase matching can lead to broadening of the XUV supercontinuum. Moreover, we also show that the bandwidth of the XUV supercontinuum can be controlled by adjusting the beam waist of the driving pulse and the position of the gas medium.

2. THEORETICAL MODEL

A. Single-Atom Model

The HHG process in atomic gases can be well understood by the single-atom response and the collective response of a

macroscopic gas to the laser and harmonic fields. In our calculation, we apply the strong-field approximation model (SFA) [51] to calculate the harmonic radiation. The time-dependent dipole momentum $d(t)$ is described as

$$d(t) = i\int_{-\infty}^{t} dt' \left[\frac{\pi}{\epsilon + i(t-t')/2}\right]^{3/2} \times d^*[p_{st}(t',t) - A(t)]d[p_{st}(t',t) - A(t')] \times \exp[-iS_{st}(t',t)]E(t')g(t') + \text{c.c.}, \quad (1)$$

where $E(t)$ is the laser field, $A(t)$ is the corresponding vector potential, and ϵ is a positive regularization constant. p_{st} and S_{st} are the stationary momentum and quasiclassical action, respectively. The $g(t)$ represents the ground-state amplitude, which is calculated by the Ammosov–Delone–Krainov (ADK) tunneling model [52]. Then the harmonic spectrum is obtained by Fourier transforming the time-dependent dipole acceleration $a(t)$,

$$a_q = \frac{1}{T}\int_0^T a(t)\exp(-iq\omega t), \quad (2)$$

where $a(t) = \ddot{d}(t)$, and T and ω are the duration and frequency of the driving pulse, respectively. q corresponds to the harmonic order. Here, it is worth mentioning that a modified ADK model [53] has been developed to calculate the harmonic spectrum more accurately. We have also employed the modified ADK theory to obtain the harmonic spectrum in our conditions. We find that the intensities of the harmonic spectra obtained by the conventional and modified ADK theory show slight differences, but the structures of the continuous harmonic spectra are nearly the same. In the following, we use the conventional ADK theory to calculate the harmonic spectrum.

B. Propagation Model

To simulate the collective response of macroscopic gas, we numerically solve the three-dimensional Maxwell wave equations for the fields of the laser pulse E_l and the harmonics E_h in cylindrical coordinates separately [54,55]. The three-dimensional Maxwell's wave equation of the laser field is expressed as

$$\nabla^2 E_l(r,z,t) - \frac{1}{c^2}\frac{\partial^2 E_l(r,z,t)}{\partial t^2} = \mu_0\frac{\partial J_{abs}(r,z,t)}{\partial t} + \frac{\omega^2}{c^2}(1-\eta_{eff}^2)E_l(r,z,t), \quad (3)$$

where $E_l(r,z,t)$ is the transverse electric field of the fundamental laser pulse with central frequency ω and z is the axial propagation direction. The effective refractive index of the gas medium can be expressed as

$$\eta_{eff}(r,z,t) = \eta_0(r,z,t) + \eta_2 I(r,z,t) - \frac{\omega_p^2(r,z,t)}{2\omega^2}, \quad (4)$$

where the linear term $\eta_0 = 1 + \delta_1 - i\beta_1$ accounts for refraction (δ_1) and absorption (β_1) by the neutral atoms, and the refraction coefficient δ_1 is obtained from the Sellmeier equation [56]. The absorption effect (β_1) on the fundamental laser field caused by the neutral atoms is neglected because it is, in general, small. The second term $\eta_2 I(r,z,t)$ describes the optical Kerr nonlinearity and the third term is from free electrons, which contains the plasma frequency

$$\omega_p = e\left[\frac{4\pi n_e(t)}{m_e}\right]^{1/2}, \quad (5)$$

where m_e and e are the mass and charge of electron, respectively. $n_e(t) = n_0[1 - \exp(-\int_{-\infty}^{t}\gamma(t')dt')]$ is the free-electron density in the gas, $\gamma(t')$ is the ionization rate, and n_0 is the density of the gas medium. $n_0(\text{m}^{-3}) = 3.5\times10^{22} * p(\text{torr})$, where p is the gas pressure. The absorption term $J_{abs}(t)$ is [57]

$$J_{abs}(t) = \frac{\gamma(t)n_e(t)I_p E_l(t)}{|E_l(t)|^2}, \quad (6)$$

where I_p is the ionization potential. Next, we only keep the real terms in the refractive index η_{eff} as well as go to a moving coordinate frame ($z' = z$, $t' = t - z/c$) and neglect $\partial^2 E_l/\partial z'^2$, then obtain [58]

$$\nabla_\perp^2 E_l(r,z',t') - \frac{2}{c}\frac{\partial^2 E_l(r,z',t')}{\partial t'\partial z'} = \mu_0\frac{\partial J_{abs}(r,z',t')}{\partial t'} + \frac{\omega_p^2}{c^2}E_l(r,z',t') - \frac{2\omega^2}{c^2}(\delta_1 + \eta_2 I)E_l(r,z',t'). \quad (7)$$

Then, we eliminate the temporal derivative in Eq. (7) by a Fourier transform and obtain the equation

$$\nabla_\perp^2 E_l'(r,z',\omega) - \frac{2i\omega}{c}\frac{\partial E_l'(r,z',\omega)}{\partial z'} = G'(r,z',\omega), \quad (8)$$

where

$$E_l'(r,z',\omega) = F'[E_l(r,z',t')], \quad (9)$$

$$G'(r,z',\omega) = F'\left[\mu_0\frac{\partial J_{abs}(r,z',t')}{\partial t'} + \frac{\omega_p^2}{c^2}E_l(r,z',t') - \frac{2\omega^2}{c^2}(\delta_1 + \eta_2 I)E_l(r,z',t')\right], \quad (10)$$

and F' is the Fourier transform operator acting on the temporal coordinate. The fundamental laser field is assumed to be Gaussian at the entrance of a gas jet.

The three-dimensional Maxwell's wave equation of the harmonic field is described by

$$\nabla^2 E_h(r,z,t) - \frac{1}{c^2}\frac{\partial^2 E_h(r,z,t)}{\partial t^2} = \mu_0\frac{\partial^2 P(r,z,t)}{\partial t^2}, \quad (11)$$

where $P(r,z,t)$ is the polarization depending upon the applied optical field $E_l(r,z,t)$. Similarly, we go to a moving coordinate frame as well as neglect $\partial^2 E_h/\partial z'^2$ and eliminate the temporal derivative by a Fourier transform, then obtain the equation

$$\nabla_\perp^2 E_h'(r,z',\omega) - \frac{2i\omega}{c}\frac{\partial E_h'(r,z',\omega)}{\partial z'} = -\omega^2\mu_0 P'(r,z',\omega), \quad (12)$$

where $E_h'(r,z',\omega) = F'[E_h(r,z',t')]$ and $P'(r,z',\omega) = F'[P(r,z',t')]$. The right-hand side of Eq. (12) describes the response of the medium to the laser field and includes both linear and nonlinear terms. $P'(r,z',\omega) = \chi^{(1)}(\omega)E_h'(r,z',\omega) + P_{nl}'(r,z',\omega)$. $P_{nl}'(r,z',\omega) = F'[(n_0 - n_e(r,z',t'))d(r,z',t')]$ is the nonlinear polarization of the medium, $n_0 - n_e(r,z',t')$ gives the density of the remaining neutral atoms, and $d(r,z',t')$ is the

single-atom induced dipole moment. The $\chi^{(1)}(\omega)$ is the linear susceptibility, which is related to the refractive index $n(\omega) = \sqrt{1+\chi^{(1)}(\omega)/\epsilon_0}$. $n(\omega) = 1 - \frac{1}{2\pi} n_0 r_0 \lambda^2 (f_1 + i f_2)$, where r_0 is the classical electron radius, λ is the wavelength, and f_1 and f_2 are atomic scattering factors. Finally, Eq. (12) can be written as

$$\nabla_\perp^2 E_h'(r,z',\omega) - \frac{2i\omega}{c}\frac{\partial E_h'(r,z',\omega)}{\partial z'} - \frac{2\omega^2}{c^2}\left(\frac{1}{2\pi} n_0 r_0 \lambda^2 (f_1 + i f_2)\right) E_h'(r,z',\omega) = -\omega^2 \mu_0 P_{nl}'(r,z',\omega). \quad (13)$$

Equations (8) and (13) can be solved with the Crank–Nicholson method. In our calculations, we adopt the radial grid with a maximum radius of 150 μm and the grid spacing Δr is 1 μm along the radial direction. The length of propagation is 1000 μm and corresponding grid spacing Δz is 2 μm along the propagation direction. In the simulations, we first calculate the single-atom dipole moment, the ionization probability, and the ionization rate on the initial plane ($z = 0$) via Eq. (1). Then, we insert the single-atom dipole moment, the ionization probability, and the ionization rate into Eqs. (3) and (11) to obtain the laser field and high-order harmonics on the next plane ($z' = z + \Delta z$). Repeating this procedure, we obtain the final high harmonics and laser field at the exit of the gas medium. In the three-dimensional model, the generated harmonics are radially distributed. In this work we only study the high harmonics at the center of the beam ($r = 0$). In this propagation model, the influence of the propagation of the laser field on the single atom response is considered while the influence of the harmonics field generated by an atom on the single-atom response of the next atom is ignored.

C. Phase Matching of High-Order Harmonic Generation

In the HHG process many macroscopic effects can give rise to the phase mismatching of high harmonics. The phase-mismatching degree can be expressed as [59,60]

$$\Delta k = \Delta k_g + \Delta k_d + \Delta k_e + \Delta k_a, \quad (14)$$

where $\Delta k_g = q \frac{2}{b[1+(2z/b)^2]}$ is the spatial phase variations arising from the focusing geometry of the laser field, q is the harmonic order, b is the confocal parameter of the beam, z is the position of the medium, and $z < 0$ and >0 mean the upstream and downstream of the laser focus. The Δk_g is independent of the time. The $\Delta k_d = \alpha_j \frac{\partial I}{\partial z}$ is the phase mismatching due to the intensity-dependent single-atom dipole phase; α_j is the phase coefficient. During the laser pulse, I and therefore Δk_d vary with time. $\Delta k_e = \frac{w}{c}\Delta n_{el}(w)$ and $\Delta k_a = \frac{w}{c}\Delta n_{at}(w)$ are due to the dispersions of the free electrons and neutrals, $\Delta n(w)$ is the difference in the refractive index, $\Delta n(w) \propto n_0 IP$ for the free electrons and $\Delta n(w) \propto n_0(1 - IP)$ for the neutrals, and IP is ionization probability. Since the ionization probability IP changes with time, Δk_e and Δk_a are time dependent. Above all, the phase-mismatching degree Δk varies with time.

3. RESULTS AND DISCUSSION

In Fig. 1, we first compare the harmonic spectra obtained on the single-atom level with that on the macroscopic level. In our simulation, we adopt an intense 800 nm laser field with the intensity of 2.0×10^{15} W/cm^2. The laser field is expressed as $E(t) = E_0 f(t)\cos(\omega t)$. Here, $f(t) = \sin^2(\frac{\pi t}{\tau})$ with duration $\tau = 7\ T_0$ (i.e., the full width at half-maximum of the pulse is 6.8 fs and T_0 is the optical cycle of the driving pulse) is the laser envelope. One can see that on the single-atom level [Fig. 1(a)], an XUV continuous spectrum with a bandwidth of 21 eV (251th–265th) is obtained near the cutoff region. Figure 1(b) shows the on-axis harmonic spectrum calculated on the macroscopic level. Here, the beam waist of the laser field is 60 μm and the gas medium neon is placed at the focus. The gas pressure is 10 Torr and the media length is 1 mm. It is clear that by considering both the single-atom response as well as the macroscopic propagation effect of the HHG a broader XUV continuum with a bandwidth of 59 eV (213th–251th) is generated.

For a better understanding of the broadening of the XUV supercontinuum on the macroscopic level we perform time-frequency analysis for the harmonic spectra in Fig. 1. The corresponding results are presented in Figs. 2(a) and 2(b), respectively. In Fig. 2(a), one can see that on the single-atom level the XUV continuous spectrum in Fig. 1(a) is dominated by the harmonic emission from peak P_2. The bandwidth of the continuum is determined by the energy difference between the highest and the second highest peaks, i.e., peaks P_2 and P_1. Since the maximum kinetic energy of P_2 is 21 eV higher than that of P_1, an XUV continuum with a bandwidth of 21 eV is generated in the region from H251 to H265 while on the macroscopic level [Fig. 2(b)] the XUV continuous spectrum is dominated by the harmonic emission from peak P_1 rather than that from peak P_2. The yields above the 213th harmonics (H213) from peak P_2 are suppressed while the harmonic emission above H213 from peak P_1 remains efficient. Therefore, an XUV continuum is produced in the region from H213 to H251 (59 eV) of peak P_1 as shown in Fig. 1(b).

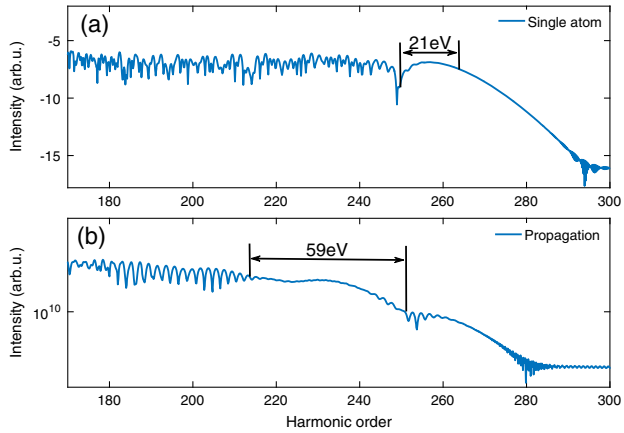

Fig. 1. Harmonic spectra obtained on (a) the single-atom level and (b) the macroscopic level. Here, the laser field is chosen as a 800 nm laser field with an intensity of 2.0×10^{15} W/cm^2. The duration of the laser field is seven cycles. The beam waist of the driving field at the focus is 60 μm, the gas pressure is 10 Torr, and the medium neon is placed at the focus.

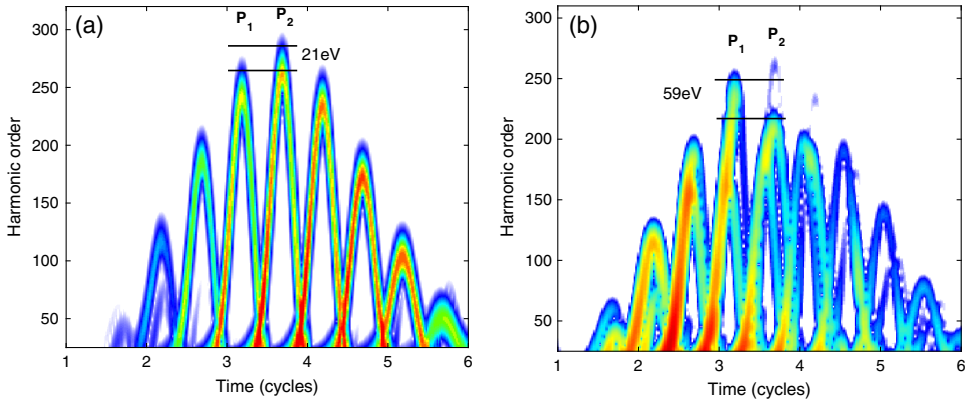

Fig. 2. (a) Time-frequency analysis for the harmonic spectrum calculated with the single-atom model. (b) Same as (a), but with the propagation model. The parameters are the same as in Fig. 1.

In order to clarify the physical mechanism of the broadening of the XUV continuum after propagation we next analyze the on-axis phase-matching conditions of the continuous harmonics. In Fig. 3(a), we present the dependence of the classical electron energy on the ionization (yellow circles) and recombination (white stars) times. One can see that, for the harmonics above H151, the electrons of peak P_1 are ionized in the region from 2.503 T_0 to 2.594 T_0. For peak P_2 the ionization of electrons occurs in the region from 3.012 T_0 to 3.104 T_0. Figure 3(b) presents the on-axis phase mismatching $|\Delta k|$ of the harmonics above H151 as a function of the time. Note that the gas medium is placed at the focus, where Δk_d is equal to 0 m^{-1} for both the short and long paths and therefore the $|\Delta k|$ of the short and long paths are the same. It is clear that the values of $|\Delta k|$ in the time interval from 2.503 T_0 to 2.594 T_0 are much smaller than those from 3.012 T_0 to 3.104 T_0.

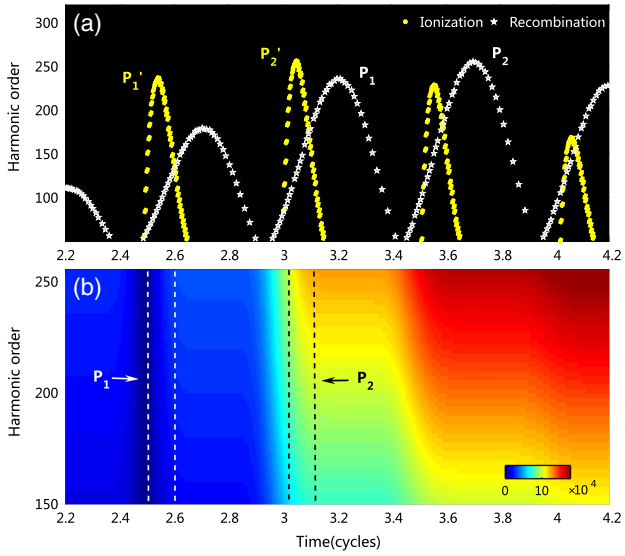

Fig. 3. (a) Harmonic order as a function of the ionization time (yellow circles) and recombination time (white stars). (b) The on-axis phase mismatching $|\Delta k|$ as a function of the time and harmonic order for the short path. Blue (red) areas correspond to good (poor) phase matching. The parameters are the same as in Figs. 1(b) and 2(b).

This indicates that the harmonic emission from peak P_1 is better phase matched than that from peak P_2. Therefore, the harmonic intensity of peak P_1 is stronger than that of peak P_2, as shown in Fig. 2(b). Moreover, in the region from 3.012 T_0 to 3.104 T_0, the $|\Delta k|$ of the harmonics above H213 are on the order of 10^5 m^{-1}, which is nearly one order of magnitude larger than those below H213. Namely, the harmonics above H213 from peak P_2 have worse on-axis phase matching than those below H213. As a consequence, for the harmonics above H213 in peak P_2, the harmonic emission is inefficient, as shown in Fig. 2(b), and then an XUV broadband continuum is generated by the harmonics from H213 to H251 (59 eV) of peak P_1, as shown in Fig. 1(b). Note that a similar macroscopical continuum is also studied in Gaarde's work [61]. There, they attributed the macroscopical continuum to the strong spatiotemporal reshaping of the laser pulse in the propagation while in our work the gas pressure is only 10 Torr, which is much lower than that in Gaarde's work (135 Torr). Therefore, the spatiotemporal reshaping of the laser pulse is much weaker in our work, which is not the main contribution to the generation of the macroscopical continuum.

In Figs. 4(a)–4(c) we show the on-axis harmonic spectra calculated with beam waists of 30 μm, 60 μm, and 100 μm, respectively. Here, the laser intensity is maintained at 2.0×10^{15} W/cm^2 for each beam waist and the other parameters are the same as in Fig. 1. The corresponding time-frequency analyses for the harmonic spectra are presented in Figs. 4(d)–4(f). With a beam waist of 30 μm, the energy difference between peaks P_1 and P_2 is nearly equal to zero, as shown in Fig. 4(d). Therefore, there is no obvious continuous structure in the harmonic spectrum, as shown in Fig. 4(a). As the beam waist increases to 60 μm, peak P_2 is suppressed and the energy difference between peaks P_1 and P_2 is enlarged to 59 eV [Fig. 4(e)]. As a consequence, the harmonic spectrum from H213 to H251 (59 eV) becomes regular and smooth, as shown in Fig. 4(b). As the beam waist further increases to 100 μm, peak P_2 is further suppressed to H197 and the energy difference between peaks P_1 and P_2 is further enlarged to 84 eV [Fig. 4(f)]. Therefore, in Fig. 4(c), one can see that a broader XUV continuum with a bandwidth of 84 eV is generated.

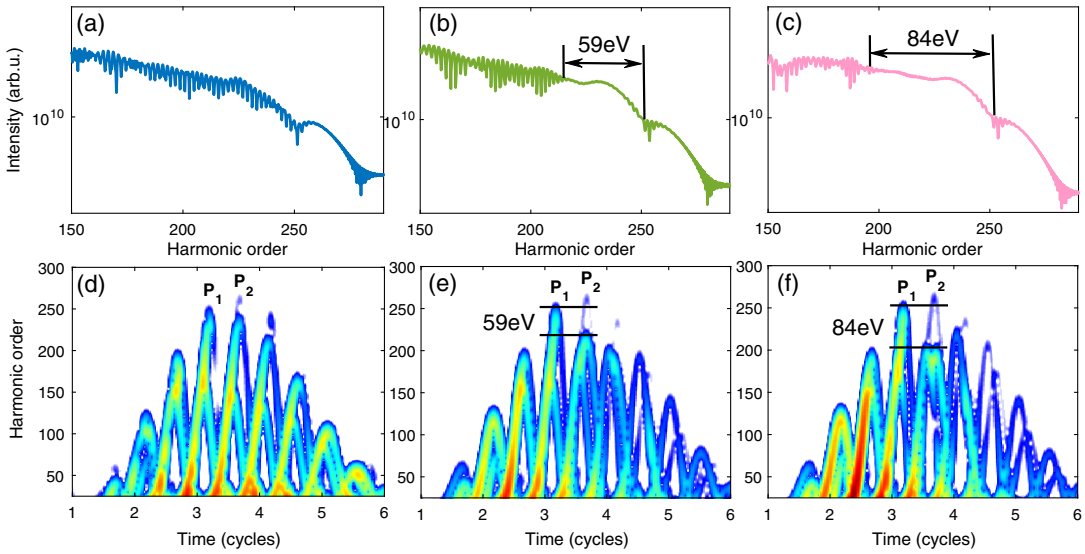

Fig. 4. (a),(d) Harmonic spectra and the corresponding time-frequency analysis with a beam waist of 30 μm. (b),(e) and (c),(f) Same as (a),(d), but for a beam waist of 60 μm and 100 μm, respectively. Other parameters are the same as in Fig. 1.

Further, we analyze the on-axis phase-matching conditions of harmonics generation with the different beam waists mentioned above. In Fig. 5(a), we present the classical electron energy as a function of the ionization (yellow circles) and recombination (white stars) times, which is the same as in Fig. 3(a). Figures 5(b)–5(d) show the on-axis phase mismatching $|\Delta k|$ of the harmonics above H151 with beam waists of 30 μm, 60 μm, and 100 μm, respectively. With a beam waist of 30 μm, the values of $|\Delta k|$ in the time interval from 2.503 T_0 to 2.594 T_0 and those in the region from 3.012 T_0 to 3.104 T_0 are all smaller than an order of 10^5 m^{-1}, as shown in Fig. 5(b). Therefore, we cannot find an obvious XUV continuous structure in the harmonic spectrum due to the small energy difference between peak P_1 and P_2 as shown in Figs. 4(a) and 4(d). With a beam waist of 60 μm, the harmonic emission from peak P_1 is still effectively phase matched while the harmonics above H213 in peak P_2 have a poor on-axis phase matching as shown in Fig. 5(c). As a consequence, an XUV continuum with a bandwidth of 59 eV is generated in the region from H213 to H251 of peak P_1 [Fig. 4(b)]. As the beam waist increased to 100 μm [Fig. 5(d)], the harmonic emission from peak P_1 had a good on-axis phase matching while for peak P_2 the harmonic emission just has good on-axis phase matching below H197. Therefore, a broadband XUV continuum is generated by the harmonics from H197 to H251 (84 eV) of peak P_1, as shown in Fig. 4(c).

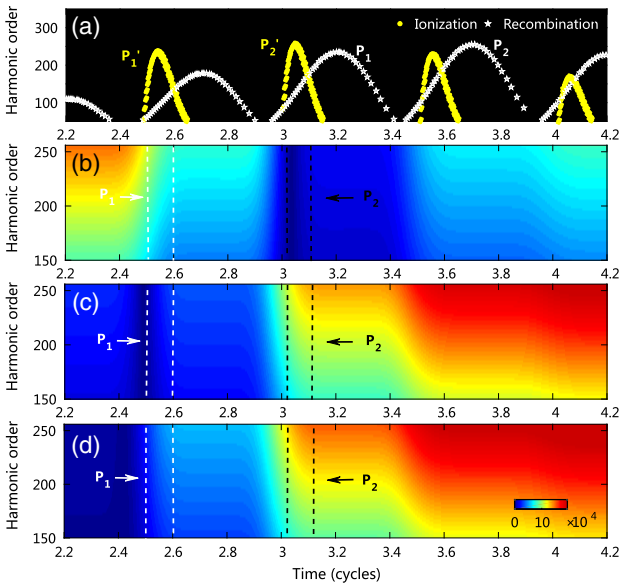

Fig. 5. (a) Harmonic order as a function of the ionization time (yellow circles) and recombination time (white stars). (b)–(d) The on-axis phase mismatching $|\Delta k|$ of the harmonics from the short path with beam waists of 30 μm, 60 μm, and 100 μm, respectively. Blue (red) areas correspond to good (poor) phase matching. The other parameters are the same as in Fig. 1.

In Figs. 6(a)–6(c), we simulate the on-axis harmonic spectra by placing the gas medium at z = −2 mm, z = 0 mm, and z = 2 mm, respectively. The corresponding time-frequency analyses for the harmonic spectra are shown in Figs. 6(d)–6(f). Here, the beam waist of the laser filed at the focus is 40 μm and the laser intensity is maintained at 2.0×10^{15} W/cm^2 for each position of the gas medium. The other parameters are the same as in Fig. 1. When the gas medium is placed at z = −2 mm the maximum kinetic energy of the P_1 is 47 eV higher than that of P_2, as shown in Fig. 6(d). Therefore, an XUV continuum with a bandwidth of 47 eV (H221–H251) is generated [Fig. 6(a)]. When the gas medium is located at z = 0 mm and z = 2 mm, the energy difference between the peaks P_1 and P_2 are both about 31 eV as shown in Figs. 6(e) and 6(f). As a consequence, a relatively narrow XUV continuum with a bandwidth of 31 eV in the region from H231 to H251 is generated [Figs. 6(b) and 6(c)].

In Fig. 7(a), we show the classical picture of HHG process, like that in Fig. 3(a). Figure 7(b) presents the on-axis phase

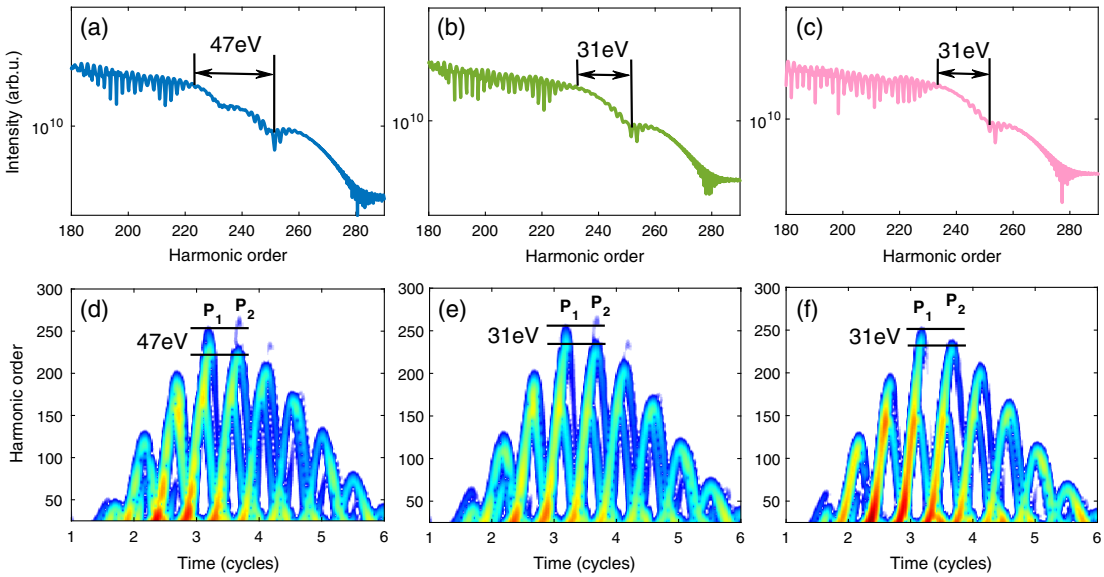

Fig. 6. (a),(d) Harmonic spectra and the corresponding time-frequency analysis calculated with the gas medium placed at z = −2 mm. (b),(e) and (c),(f) Same as (a),(d), but for the gas medium placed at z = 0 mm and z = 2 mm, respectively. Here, the beam waist of the driving field at the focus is 40 μm, and other parameters are the same as in Fig. 1.

mismatching |Δk| of the harmonics above H151 with the gas medium placed at z = −2 mm. One can see that the harmonic emission from the peak P_1 is effectively phase matched, while that from the peak P_2 just has good on-axis phase matching below H221. Therefore, a XUV continuum with a bandwidth of 47 eV (H221–H251) is generated as shown in Fig. 6(a). For the results with the gas medium placed at z = 0 mm [Fig. 7(c)] and z = 2 mm [Fig. 7(d)], the harmonic emissions from the peak P_1 are both well phase matched and those from the peak P_2 both have good on-axis phase matching below H231. As a consequence, the XUV continuum with a bandwidth of 31 eV (H231–H251) is generated as shown in Figs. 6(b) and 6(c).

Finally, the influence of the laser intensity on the technique based on the time-dependent phase matching is also studied. We find that the technique is feasible with the laser intensity above 1.5×10^{15} W/cm^2. Moreover, we have also studied the influence of the carrier-envelope phase (CEP) on this technique. We find that this technique is robust with 100 mrad CEP fluctuations.

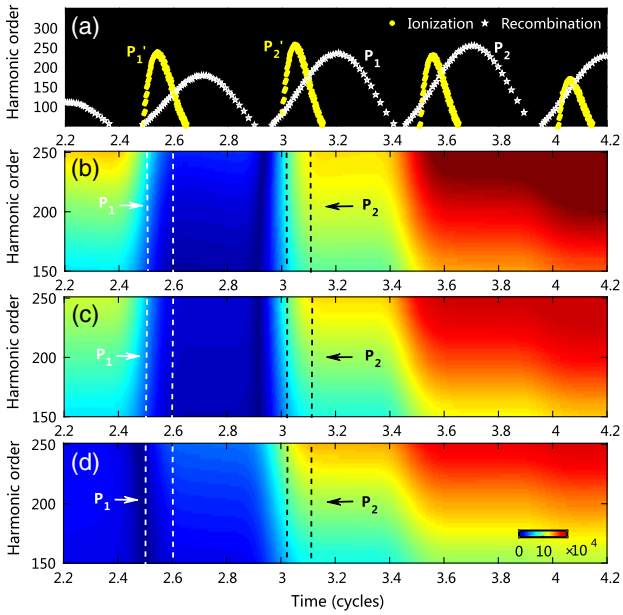

Fig. 7. (a) Harmonic order as a function of the ionization time (yellow circles) and recombination time (white stars). (b) The on-axis phase mismatching |Δk| of the harmonics from the short path with the gas medium placed at z = −2 mm. (c) and (d) Same as (a), but for the gas medium placed at z = 0 mm and z = 2 mm, respectively. Blue (red) areas correspond to good (poor) phase matching. The other parameters are the same as in Fig. 1.

4. CONCLUSION

In conclusion, we investigate the influence of the time-dependent on-axis phase matching on XUV supercontinuum generation in a low-pressure and high-intensity regime. The results show that the time-dependent on-axis phase matching can lead to broadening of the XUV supercontinuum. Moreover, we also study the influence of the beam waist and the position of the gas medium on the bandwidth of the XUV supercontinuum. We find that with the beam waist increased the harmonic emissions from the highest peak P_2 are gradually suppressed and then the bandwidth of the XUV supercontinuum is gradually broadened. When the gas medium is placed before the focus, the bandwidth of the XUV supercontinuum will be further broadened while when the gas medium is placed after the focus, the bandwidth of the XUV supercontinuum is almost unchanged.

Funding. National Natural Science Foundation of China (NSFC) (11204222); Natural Science Foundation of Hubei Province, China (2013CFB316, 2014CFB793).

Acknowledgment. Numerical simulations presented in this paper were carried out using the High Performance Computing experimental testbed in the Service Computing Technology (HPCC) and System Lab/Cluster and Grid Computing Laboratory (SCTS/CGCL).

REFERENCES

1. A. McPherson, G. Gibson, H. Jara, U. Johann, T. S. Luk, I. A. McIntyre, K. Boyer, and C. K. Rhodes, "Studies of multiphoton production of vacuum-ultraviolet radiation in the rare gases," J. Opt. Soc. Am. B **4**, 595–601 (1987).
2. E. Goulielmakis, Z. Loh, A. Wirth, R. Santra, N. Rohringer, V. S. Yakovlev, S. Zherebtsov, T. Pfeifer, A. M. Azzeer, M. F. Kling, S. R. Leone, and F. Krausz, "Real-time observation of valence electron motion," Nature **466**, 739–743 (2010).
3. M. Li, P. Zhang, S. Luo, Y. Zhou, Q. Zhang, P. Lan, and P. Lu, "Selective enhancement of resonant multiphoton ionization with strong laser fields," Phys. Rev. A **92**, 063404 (2015).
4. Y. Zhou, O. I. Tolstikhin, and T. Morishita, "Near-forward rescattering photoelectron holography in strong-field ionization: extraction of the phase of the scattering amplitude," Phys. Rev. Lett. **116**, 173001 (2016).
5. A. Tong, Y. Zhou, and P. Lu, "Resolving subcycle electron emission in strong-field sequential double ionization," Opt. Express **23**, 15774–15783 (2015).
6. X. Ma, Y. Zhou, and P. Lu, "Multiple recollisions in strong-field nonsequential double ionization," Phys. Rev. A **93**, 013425 (2016).
7. Y. Chen, Y. Zhou, Y. Li, M. Li, P. Lan, and P. Lu, "The contribution of the delayed ionization in strong-field nonsequential double ionization," J. Chem. Phys. **144**, 024304 (2016).
8. M. He, Y. Li, Y. Zhou, M. Li, and P. Lu, "Temporal and spatial manipulation of the recolliding wave packet in strong-field photoelectron holography," Phys. Rev. A **93**, 033406 (2016).
9. S. Baker, J. S. Robinson, C. A. Haworth, H. Teng, R. A. Smith, C. C. Chirilă, M. Lein, J. W. G. Tisch, and J. P. Marangos, "Probing proton dynamics in molecules on an attosecond time scale," Science **312**, 424–427 (2006).
10. Z. Wang, M. Li, Y. Zhou, Y. Li, P. Lan, and P. Lu, "Counterintuitive energy shifts in joint electron-nuclear-energy spectra of strong-field fragmentation of H_2^+," Phys. Rev. A **93**, 013418 (2016).
11. C. Huang, P. Lan, Y. Zhou, Q. Zhang, K. Liu, and P. Lu, "Tunneling site of electrons in strong-field-enhanced ionization of molecules," Phys. Rev. A **90**, 043420 (2014).
12. C. Zhai, L. He, P. Lan, X. Zhu, Y. Li, F. Wang, W. Shi, Q. Zhang, and P. Lu, "Coulomb-corrected molecular orbital tomography of nitrogen," Sci. Rep. **6**, 23236 (2016).
13. X. Zhu, P. Lan, K. Liu, Y. Li, X. Liu, Q. Zhang, I. Barth, and P. Lu, "Helicity sensitive enhancement of strong-field ionization in circularly polarized laser fields," Opt. Express **24**, 4196–4209 (2016).
14. A. L. Cavalieri, N. Müller, T. H. Uphues, V. S. Yakovlev, A. Baltuška, B. Horvath, B. Schmidt, L. Blümel, R. Holzwarth, S. Hendel, M. Drescher, U. Kleineberg, P. M. Echenique, R. Kienberger, F. Krausz, and U. Heinzmann, "Attosecond spectroscopy in condensed matter," Nature **449**, 1029–1032 (2007).
15. M. Hentschel, R. Kienberger, C. Spielmann, G. A. Reider, N. Milosevic, T. Brabec, P. Corkum, U. Heinzmann, M. Drescher, and F. Krausz, "Attosecond metrology," Nature **414**, 509–513 (2001).
16. M. Drescher, M. Hentschel, R. Kienberger, M. Uiberacker, V. Yakovlev, A. Scrinzi, T. H. Westerwalbesloh, U. Kleineberg, U. Heinzmann, and F. Krausz, "Time-resolved atomic inner-shell spectroscopy," Nature **419**, 803–807 (2002).
17. F. Krausz and M. Ivanov, "Attosecond physics," Rev. Mod. Phys. **81**, 163–234 (2009).
18. M. E. Siemens, Q. Li, R. Yang, K. A. Nelson, E. H. Anderson, M. M. Murnane, and H. C. Kapteyn, "Quasi-ballistic thermal transport from nanoscale interfaces observed using ultrafast coherent soft X-ray beams," Nat. Mater. **9**, 26–30 (2010).
19. S. A. Rezvani, Q. Zhang, Z. Hong, and P. Lu, "Tunable broadband intense IR pulse generation at non-degenerate wavelengths using group delay compensation in a dual-crystal OPA scheme," Opt. Express **24**, 11187–11198 (2016).
20. P. Corkum, "Plasma perspective on strong field multiphoton ionization," Phys. Rev. Lett. **71**, 1994–1997 (1993).
21. E. Goulielmakis, M. Schultze, M. Hofstetter, V. S. Yakovlev, J. Gagnon, M. Uiberacker, A. L. Aquila, E. M. Gullikson, D. T. Attwood, R. Kienberger, F. Krausz, and U. Kleineberg, "Single-cycle nonlinear optics," Science **320**, 1614–1617 (2008).
22. P. B. Corkum, N. H. Burnett, and M. Y. Ivanov, "Subfemtosecond pulses," Opt. Lett. **19**, 1870–1872 (1994).
23. M. Ivanov, P. B. Corkum, T. Zuo, and A. Bandrauk, "Routes to control of intense-field atomic polarizability," Phys. Rev. Lett. **74**, 2933–2936 (1995).
24. G. Sansone, E. Benedetti, F. Calegari, C. Vozzi, L. Avaldi, R. Flammini, L. Poletto, P. Villoresi, C. Altucci, R. Velotta, S. Stagira, S. D. Silvestri, and M. Nisoli, "Isolated single-cycle attosecond pulses," Science **314**, 443–446 (2006).
25. Z. Chang, "Single attosecond pulse and XUV supercontinuum in the high-order harmonic plateau," Phys. Rev. A **70**, 043802 (2004).
26. Z. Chang, "Chirp of the single attosecond pulse generated by a polarization gating," Phys. Rev. A **71**, 023813 (2005).
27. P. Lan, P. Lu, W. Cao, Y. Li, and X. Wang, "Isolated sub-100-attosecond pulse generation via controlling electron dynamics," Phys. Rev. A **76**, 011402(R) (2007).
28. H. Mashiko, S. Gilbertson, M. Chini, X. Feng, C. Yun, H. Wang, S. D. Khan, S. Chen, and Z. Chang, "Extreme ultraviolet supercontinua supporting pulse durations of less than one atomic unit of time," Opt. Lett. **34**, 3337–3339 (2009).
29. W. Hong, P. Wei, Q. Zhang, S. Wang, and P. Lu, "Mid-infrared modulated polarization gating for ultra-broadband supercontinuum generation," Opt. Express **18**, 11308–11315 (2010).
30. T. Pfeifer, L. Gallmann, M. J. Abel, D. M. Neumark, and S. R. Leone, "Single attosecond pulse generation in the multicycle-driver regime by adding a weak second-harmonic field," Opt. Lett. **31**, 975–977 (2006).
31. Z. Zeng, Y. Cheng, X. Song, R. Li, and Z. Xu, "Generation of an extreme ultraviolet supercontinuum in a two-color laser field," Phys. Rev. Lett. **98**, 203901 (2007).
32. Y. Zheng, Z. Zeng, P. Zou, L. Zhang, X. Li, P. Liu, R. Li, and Z. Xu, "Dynamic chirp control and pulse compression for attosecond high-order harmonic emission," Phys. Rev. Lett. **103**, 043904 (2009).
33. L. He, Y. Li, Q. Zhang, and P. Lu, "Ultra-broadband water window supercontinuum generation with high efficiency in a three-color laser field," Opt. Express **21**, 2683–2692 (2013).
34. P. Lan, P. Lu, W. Cao, Y. Li, and X. Wang, "Attosecond ionization gating for isolated attosecond electron wave packet and broadband attosecond xuv pulses," Phys. Rev. A **76**, 051801(R) (2007).
35. H. Mashiko, S. Gilbertson, C. Li, S. D. Khan, M. M. Shakya, E. Moon, and Z. Chang, "Double optical gating of high-order harmonic generation with carrier-envelope phase stabilized lasers," Phys. Rev. Lett. **100**, 103906 (2008).
36. M. Uiberacker, T. H. Uphues, M. Schultze, A. J. Verhoef, V. Yakovlev, M. F. Kling, J. Rauschenberger, N. M. Kabachnik, H. Schröder, M. Lezius, K. L. Kompa, H.-G. Muller, M. J. J. Vrakking, S. Hendel, U. Kleineberg, U. Heinzmann, M. Drescher, and F. Krausz, "Attosecond real-time observation of electron tunnelling in atoms," Nature **446**, 627–632 (2007).
37. E. Goulielmakis, M. Uiberacker, R. Kienberger, A. Baltuska, V. Yakovlev, A. Scrinzi, T. H. Westerwalbesloh, U. Kleineberg, U. Heinzmann, M. Drescher, and F. Krausz, "Direct measurement of light waves," Science **305**, 1267–1269 (2004).
38. R. Kienberger, E. Goulielmakis, M. Uiberacker, A. Baltuska, V. Yakovlev, F. Bammer, A. Scrinzi, T. H. Westerwalbesloh, U. Kleineberg, U. Heinzmann, M. Drescher, and F. Krausz, "Atomic transient recorder," Nature **427**, 817–821 (2004).
39. C. A. Haworth, L. E. Chipperfield, J. S. Robinson, P. L. Kninght, J. P. Marangos, and J. W. G. Tisch, "Half-cycle cutoffs in harmonic spectra and robust carrier-envelope phase retrieval," Nat. Phys. **3**, 52–57 (2007).
40. T. Auguste, P. Saliéres, A. S. Wyatt, A. Monmayrant, I. A. Walmsley, E. Cormier, A. Zaïr, M. Holler, A. Guandalini, F. Schapper, J. Biegert,

L. Gallmann, and U. Keller, "Theoretical and experimental analysis of quantum path interferences in high-order harmonic generation," Phys. Rev. A **80**, 033817 (2009).
41. A. ZaÏr, M. Holler, A. Guandalini, F. Schapper, J. Biegert, L. Gallmann, U. Keller, A. S. Wyatt, A. Monmayrant, I. A. Walmsley, E. Cormier, T. Auguste, J. P. Caumes, and P. Salières, "Quantum path interferences in high-order harmonic generation," Phys. Rev. Lett. **100**, 143902 (2008).
42. E. Brunetti, R. Issac, and D. A. Jaroszynski, "Quantum path contribution to high-order harmonic spectra," Phys. Rev. A **77**, 023422 (2008).
43. L. He, P. Lan, Q. Zhang, C. Zhai, F. Wang, W. Shi, and P. Lu, "Spectrally resolved spatiotemporal features of quantum paths in high-order-harmonic generation," Phys. Rev. A **92**, 043403 (2015).
44. E. Mével, E. Constant, D. Garzella, P. Breger, C. Dorrer, C. L. Blanc, F. Salin, and P. Agostini, "Optimizing high order harmonic generation in absorbing gases," AIP Conf. Proc. **525**, 373–384 (2000).
45. V. V. Strelkov, E. Mével, and E. Constant, "Generation of isolated attosecond pulses by spatial shaping of a femtosecond laser beam," New J. Phys. **10**, 083040 (2008).
46. E. Constant, A. Dubrouil, O. Hort, S. Petit, D. Descamps, and E. Mével, "Spatial shaping of intense femtosecond beams for the generation of high-energy attosecond pulses," J. Phys. B **45**, 074018 (2012).
47. S. Kazamias, D. Douillet, C. Valentin, F. Weihe, F. Augé, T. H. Lefrou, G. Grillon, S. Sebban, and P. H. Balcou, "Observation of high-contrast coherence fringes in high-order harmonic generation," Phys. Rev. A **68**, 033819 (2003).
48. S. Kazamias, D. Douillet, F. Weihe, C. Valentin, A. Rousse, S. Sebban, G. Grillon, F. Augé, D. Hulin, and P. H. Balcou, "Global optimization of high harmonic generation," Phys. Rev. Lett. **90**, 193901 (2003).
49. M. J. Abel, T. Pfeifer, P. M. Nagel, W. Boutu, M. J. Bell, C. P. Steiner, D. M. Neumark, and S. R. Leone, "Isolated attosecond pulses from ionization gating of high-harmonic emission," Chem. Phys. **366**, 9–14 (2009).
50. M. Chen, C. Mancuso, C. Hernández-García, F. Dollar, B. Galloway, D. Popmintchev, P. Huang, B. Walker, L. Plaja, A. Jaroń-Becker, A. Becker, M. Murnane, H. Kapteyn, and T. Popmintchev, "Generation of bright isolated attosecond soft X-ray pulses driven by multicycle midinfrared lasers," Proc. Natl. Acad. Sci. USA **111**, E2361–E2367 (2014).
51. M. Lewenstein, P. H. Balcou, M. Y. U. Ivanov, A. L'Huillier, and P. B. Corkum, "Theory of high-harmonic generation by low-frequency laser fields," Phys. Rev. A **49**, 2117–2132 (1994).
52. M. V. Ammosov, N. B. Delone, and V. P. Krainov, "Tunnel ionization of complex atoms and of atomic ions in an alternating electric field," Sov. Phys. J. Exp. Theor. Phys. **64**, 1191–1194 (1986).
53. X. M. Tong and C. D. Lin, "Empirical formula for static field ionization rates of atoms and molecules by lasers in the barrier-suppression regime," J. Phys. B **38**, 2593–2600 (2005).
54. P. Lan, P. Lu, Q. Li, F. Li, W. Hong, and Q. Zhang, "Macroscopic effects for quantum control of broadband isolated attosecond pulse generation with a two-color field," Phys. Rev. A **79**, 043413 (2009).
55. C. Jin, A. Le, and C. D. Lin, "Medium propagation effects in high-order harmonic generation of Ar and N_2," Phys. Rev. A **83**, 023411 (2011).
56. A. Börzsönyi, Z. Heiner, M. P. Kalashnikov, A. P. Kovács, and K. Osvay, "Dispersion measurement of inert gases and gas mixtures at 800 nm," Appl. Opt. **47**, 4856–4863 (2008).
57. M. B. Gaarde, J. L. Tate, and K. J. Schafer, "Macroscopic aspects of attosecond pulse generation," J. Phys. B **41**, 132001 (2008).
58. E. Priori, G. Cerullo, M. Nisoli, S. Stagira, S. De Silvestri, P. Villoresi, L. Poletto, P. Ceccherini, C. Altucci, R. Bruzzese, and C. de Lisio, "Nonadiabatic three-dimensional model of high-order harmonic generation in the few-optical-cycle regime," Phys. Rev. A **61**, 063801 (2000).
59. F. Wang, L. He, C. Zhai, W. Shi, Q. Zhang, P. Lan, and P. Lu, "Time-dependent phase matching of high-order-harmonic generation," Phys. Rev. A **92**, 063839 (2015).
60. P. Balcou, P. Salières, A. L'Huillier, and M. Lewenstein, "Generalized phase-matching conditions for high harmonics: the role of field-gradient forces," Phys. Rev. A **55**, 3204–3210 (1997).
61. M. B. Gaarde and K. J. Schafer, "Generating single attosecond pulses via spatial filtering," Opt. Lett. **31**, 3188–3190 (2006).